Atmos. Meas. Tech. Discuss., 5, 6455–6478, 2012
www.atmos-meas-tech-discuss.net/5/6455/2012/
doi:10.5194/amtd-5-6455-2012

Atmospheric Measurement Techniques Discussions

Esrange lidar's new pure rotational-Raman channel for measurement of temperature and aerosol extinction in the troposphere and lower stratosphere

P. Achtert, M. Khaplanov, F. Khosrawi, and J. Gumbel

Department of Meteorology, Stockholm University, Stockholm, Sweden

Received: 5 July 2012 – Accepted: 25 August 2012 – Published: 7 September 2012

Correspondence to: P. Achtert (peggy@misu.su.se)

Published by Copernicus Publications on behalf of the European Geosciences Union.

Abstract

The Department of Meteorology at Stockholm University operates the Esrange Rayleigh/Raman lidar at Esrange (68° N, 21° E) near the Swedish city of Kiruna. This paper describes the design and first measurements of the new pure rotational-Raman channel of the Esrange lidar. The Esrange lidar uses a pulsed Nd:YAG solid-state laser operating at 532 nm as light source with a repetition rate of 20 Hz and a pulse energy of 350 mJ. The minimum vertical resolution 150 m and the integration time for one profile is 5000 shots. The newly implemented channel allows for measurements of atmospheric temperature at altitudes below 35 km and is currently optimized for temperature measurements between 180 and 200 K. This corresponds to conditions in the lower Arctic stratosphere during winter. In addition to the temperature measurements the aerosol extinction coefficient and the aerosol backscatter coefficient at 532 nm can be measured independently. Our filter-based design minimizes the systematic error in the obtained temperature profile to less than 0.51 K. By combining rotational-Raman measurements (5–35 km height) and the integration technique (30–80 km height), the Esrange lidar is now capable of measuring atmospheric temperature profiles from the lower troposphere up to the mesosphere. With the improved setup, the system can be used to validate current lidar-based polar stratospheric cloud classification schemes. The new capability of the instrument measuring temperature and aerosol extinction furthermore enables studies of the thermal structure and variability of the upper troposphere/lower stratosphere. Although several lidars are operated at polar latitudes, there are few instruments that are capable to measure temperature profiles in the troposphere, stratosphere, and mesosphere, as well as aerosols extinction in the troposphere and lower stratosphere with daylight capability.

1 Introduction

Temperature is a key parameter of the state of the atmosphere. Knowledge of atmospheric temperature helps to identify and understand climatological, meteorological, and dynamical processes. A variety of techniques can be applied to obtain temperature profiles from lidar measurements. Each of these techniques covers a certain height range: differential absorption lidar (for observations in the boundary layer), rotational-Raman and high-spectral-resolution lidar (from the ground to the upper stratosphere), vibrational-Raman lidar (from the upper troposphere and lower stratosphere), the integration technique (from the middle stratosphere up to the mesopause), and the resonance-fluorescence technique (from the mesopause region to the lower thermosphere). Detailed information about the different techniques can be found in Behrendt (2005). The rotational-Raman technique in combination with the integration technique can be used to cover an altitude range from the ground to the mesopause and allows for the observation of diurnal and wave-related variations as well as small-scale vertical structures of atmospheric temperature. Such information is necessary to understand meteorological processes, e.g. the propagation of gravity waves and the formation of tropospheric and stratospheric clouds.

In the winter stratosphere polar stratospheric clouds (PSCs) provide the surface for heterogeneous reactions which transform stable chlorine and bromine species into their highly reactive ozone-destroying states. PSCs are classified into three types (PSC Ia: nitric acid di- or trihydrate crystals, NAD or NAT; PSC Ib: supercooled liquid ternary solutions, STS; PSC II: ice) according to their particle composition and to their physical phase (McCormick et al., 1982; Poole and McCormick, 1988). The formation of PSCs (in particular that of ice PSCs) is strongly controlled by the detailed structure of the temperature profile. In the Arctic stratosphere gravity-wave-induced temperature modifications play an important role, since synoptic processes are not as sufficient for producing the temperatures necessary for PSC formation as in the Antarctic (Carslaw et al., 1998; Dörnbrack et al., 2000; Höpfner et al., 2001; Blum et al., 2005; Juarez et al., 2009). However, Wang et al. (2008) and Achtert et al. (2012) showed that the formation of PSCs can also be associated with underlying deep-tropospheric clouds. These cloud systems affect PSC formation because they can cause adiabatic cooling in the lower stratosphere. This cooling effect can affect both PSC formation and microphysical properties, i.e. PSC type (Adhikari et al., 2010).

For a comprehensive understanding of such temperature-dependent processes in the stratosphere, the rotational-Raman technique is most suitable. In contrast to the integration technique, it allows for temperature measurements also in the presence of aerosol layers and clouds (Cooney et al., 1972). The integration technique can only be applied if the hydrostatic equilibrium equation and the ideal gas law are valid. It involves integrating the relative density profile in an aerosol-free atmosphere downward using a starting temperature at an upper altitude. Another method to extend the temperature retrieval to heights below 30 km is the vibrational-Raman technique (Keckhut et al., 1990; Hauchecorne et al., 1992). However, detailed information on aerosols, clouds, and ozone concentration is required to obtain temperature profiles with reasonable uncertainty (Faduilhe et al., 2005).

This paper is structured as follows: first we will give a description of the design and operation of the new channel in Sects. 2 and 3, respectively. First measurement results are presented in Sect. 4. The paper closes with conclusion and outlook in Sect. 5.

2 The Esrange lidar

The Department of Meteorology of the Stockholm University operates the Esrange lidar at Esrange (68° N, 21° E) near the Swedish city of Kiruna. It was originally installed in 1997 by the University of Bonn (Blum and Fricke, 2005). The Esrange lidar uses a pulsed Nd:YAG solid-state laser operating at 532 nm as light source. The Rayleigh/Raman lidar has so far provided stratospheric and mesospheric measurements of clouds, aerosols, and temperatures (integration technique, from the middle stratosphere up to the mesopause). Recent scientific studies applying measurements from the Esrange lidar have been presented by Achtert et al. (2011) and Khosrawi et al. (2011). In addition the Esrange lidar is used to identify favorable launch conditions in connection with balloon and rocket campaigns at Esrange (Gumbel , 2007). The extension of the system with a rotational-Raman channel allows for accurate high-resolution temperature measurements between 5 and 35 km which is important for an improved characterization of clouds (such as PSCs) and aerosol layers. It will furthermore be useful for studying the thermal structure and variability of the high-latitude upper troposphere and stratosphere.

2.1 Emitter side

The emitter side of the lidar consists of a pulsed solid state Nd:YAG laser with a repetition rate of 20 Hz. Currently, only the frequency-doubled light (532 nm) is emitted. A beam widening telescope expands the beam diameter from 9 mm to 9 cm before a steerable mirror directs the beam vertically into the atmosphere. The beam expansion leads to a reduced divergence from 500 µrad to 50 µrad. More information about the optical setup of the emitter side can be found in Blum and Fricke (2005). The emitter properties are given in Table 1.

2.2 Receiver side

The Esrange lidar uses three Newtonian telescopes with an individual mirror diameter of 50.8 cm and a focal length of 254.0 cm. For each telescope backscattered light is collected into one focal box where it is separated according to wavelength and state of polarization (for more information, see Blum and Fricke, 2005). From there optical fibers are used to guide the light to the detector. In standard configuration, identical focal boxes (separating 532 nm parallel, 532 nm perpendicular, and 608 nm) are used for all three telescopes. In this way, the total signal is maximized. It is also possible to

AMTD
5, 6455–6478, 2012

attach different focal boxes that are optimized for different wavelengths to the individual telescopes. In January/February 1999 the focal box of one of the telescopes was optimized for receiving rotational-Raman signals (Behrendt et al., 1999). However, this approach of altering only one focal box strongly affects the signal strength.

For high resolution temperature measurements within aerosol layers and clouds, the elastic-backscatter signal has to be blocked sufficiently. Besides the blocking efficiency, the center wavelength and channel passband of the applied filters are important to yield minimum statistical errors within the height-region of interest. The parameters for the rotational-Raman channel of the Esrange lidar were chosen to optimize temperature measurements in the lower Arctic winter stratosphere.

In the new setup presented here a reflection from the interference filters in both parallel and perpendicular optical branches is used to extract rotational-Raman signals from the combined light detected with all three telescopes (Fig. 1a). This approach maximizes the detected signal and furthermore enables a separation of the rotational-Raman scattering from the elastic backscatter signal. Both interference filters have a central wavelength (CWL) of 532.13 nm and a full width at half maximum (FWHM) of 0.13 nm (Table 1). The reflected light from both interference filters is guided through a prism (not shown in Fig. 1a) into one optical fiber each and transported simultaneously to the rotational-Raman bench (Fig. 1a). The optical setup of the rotational-Raman channel is shown in Fig. 1b. This design enables to adjust the CWL by varying the tilting angles of the filters. Due to the sequential mount of the two rotational-Raman channels a high suppression of at least 10 orders of magnitude of the elastic signal is achieved. Such suppression is necessary because the transmission band of R-IF2 is very close to the laser wavelength. The characteristics of the filters is listed in Table 2. The values are taken from manufacturer's data sheet (Barr Associates, MA, USA). Figure 2 shows the extracted anti-Stokes branch and the transmission curves of the manufactured filters. The rotational-Raman spectrum for O_2 and N_2 for a temperature of $T_1 = 180$ K and $T_2 = 200$ K was calculated as described in Nedeljkovic et al. (1993) and Radlach et al. (2008). These values correspond to minimum and maximum temperatures in the wintertime Arctic stratosphere, respectively. The filter specification was selected according to the method described by Behrendt (2005) and Radlach et al. (2008) with:

$$\Delta T = \frac{\delta T}{\delta Q}\Delta Q \approx \frac{T_1 - T_2}{Q_1 - Q_2} Q \sqrt{\frac{P_{\mathrm{RR1}} + 2P_{\mathrm{B1}}}{P_{\mathrm{RR2}}^2} + \frac{P_{\mathrm{RR2}} + 2P_{\mathrm{B2}}}{P_{\mathrm{RR1}}^2}}. \tag{1}$$

Here, Q is the ratio between the two background corrected rotational-Raman signals P_{RR1} and P_{RR2} with:

$$Q(T,z) = \frac{P_{\mathrm{RR2}}(T,z)}{P_{\mathrm{RR1}}(T,z)}. \tag{2}$$

Q_1 and Q_2 are the corresponding ratios for both rotational-Raman signals at a different temperature. P_{B1} and P_{B2} are the total background signals of each channel. ΔT has a minimum for a certain temperature range depending on the signal intensities. These in turn depend on ambient temperature and background intensity. The CWL's of the interference filters were chosen in a way that the transmission curve of the filter close to the central wavelength (with all possible manufactured uncertainties from CWL and FWHM) only includes the first three rotational-Raman lines of O_2 and N_2. There are two advantages to this design. First, the statistical temperature uncertainty is smaller when more than one rotational-Raman line is included (Radlach et al., 2008). Second, the statistical temperature uncertainty for T_1 = 180 K and T_2 = 200 K is higher when the fourth rotational-Raman line would be included. For PSCs the optimum central wavelength (CWL) lines are $\mathrm{CWL_{RR1}}$ = 531.55 nm and $\mathrm{CWL_{RR2}}$ = 529.35 nm. The temperature sensitivity for these two lines is 0.51 K. Both chosen CWLs in our system are in the same region as the CWLs ($\mathrm{CWL_{RR1}}$ = 531.7 nm and $\mathrm{CWL_{RR2}}$ = 529.35 nm same, FWHMs as our system) suggested for measurements within PSCs by Behrendt (2005). The optimum filter parameters for CWL2 are very close to the elastic backscatter line and require a high suppression. The manufactured filters by Barr Associated Inc. have an suppression of at least 10 orders of magnitude.

The aerosol backscatter coefficient β_{aer} and the aerosol extinction coefficient α_{aer} can be determined using a Raman signal (weighted sum of both signals) and one elastic signal (Behrendt et al., 2002; Ansmann and Müller, 2005). The aerosol backscatter coefficient can be calculated as:

$$\beta_{aer}(\lambda_0,R) = -\beta_{mol}(\lambda,R) + (\beta_{aer}(\lambda_0,R_0) + \beta_{mol}(\lambda_0,R_0))\frac{P(\lambda_{RR},R_0)P(\lambda_0,R)N(R)}{P(\lambda_{RR},R)P(\lambda_0,R_0)N(R_0)}, \quad (3)$$

and the aerosol extinction coefficient as:

$$\alpha_{aer}(R) = \frac{1}{2}\frac{d}{dz}\left(\ln\frac{N(R)}{P(\lambda_{RR},R_0)R^2}\right) - \alpha_{mol}(R). \quad (4)$$

Here $P(\lambda_{RR},R)$ is the weighted sum of both rotational-Raman signals. Before processing, all detected signals are corrected for background and range (R) effects. The molecular number concentration N, the molecular backscatter coefficient β_{mol}, and the molecular extinction coefficient α_{mol} can be calculated from standard atmosphere or radiosonde (Bucholtz, 1995). A value for the backscatter coefficient at a reference height R_0 has to be chosen where the aerosol backscattering is typically negligible compared to Rayleigh scattering. The lidar ratio is the ratio of aerosol extinction and aerosol backscatter coefficient.

3 Data analysis

For a standard measurement we use a detection range gate of 1 µs which results in a vertical resolution of 150 m. Typically, 5000 laser shorts are integrated which results in an temporal resolution of about 5 min. Measurements of backscattered signals polarized parallel and perpendicular to the plane of polarization of the emitted laser light are used to derive the backscatter ratio R, the aerosol backscatter coefficient β_{aer}, and the linear aerosol depolarization ratio δ_{aer}. The molecular fraction of the received signal is determined either from the signal above the clouds or by use of a concurrent

AMTD
5, 6455–6478, 2012
Rotational-Raman channel of Esrange lidar
P. Achtert et al.

temperature and pressure reanalysis. The molecular signal has to be normalized to the Rayleigh signal in the aerosol-free part of the atmosphere to calculate the absolute value of the backscatter ratio. For the spectral bandpass of the detector, the value of the molecular depolarization ratio is $\delta_{\mathrm{mol}} = 0.0036$ (Blum and Fricke, 2005).

The ratio Q of the pure rotational-Raman backscatter signals at 529.45 and 531.55 nm has to be calibrated with temperature profiles measured with radiosondes or from reanalysis data to obtain accurate atmospheric temperature profiles from the lidar measurements. During a measurements campaign in January/February 2011 eight radiosondes for the comparison were launched from Esrange and reached altitudes between 15 and 30 km. In total 13 temperature measurements were conducted during this campaign. The functional relation between temperature T and the ratio Q can be described with a linear or quadratic fit as:

$$Q(T,R) = \exp\left(\frac{A}{T(R)} + B\right), \quad \text{or} \tag{5}$$

$$Q(T,R) = \exp\left(\frac{A}{T(R)^2} + \frac{B}{T(R)} + C\right), \tag{6}$$

respectively. A, B, and C are calibration constants. The conducted calibrations showed that the quadratic relationship agrees better than the simple linear fit for our measurements. As described in Behrendt (2005) Eq. (6) yields better results for a wider range of temperature (≈ 50 K). Inverting Eq. (6) leads to an equation for the temperature

$$T(z) = \frac{-2A}{B \pm \sqrt{B^2 - 4A(C - \ln[Q(T,R)])}} \tag{7}$$

which is applied to our atmospheric measurements. Large extrapolation errors can be avoided by using a least square fitting function.

The raw counts of the two rotational-Raman channels and the temperature profile derived between 03:17 and 07:58 UT on 20 January 2011 are shown in Fig. 3a and

AMTD
5, 6455–6478, 2012

b, respectively. A radiosonde was launched from Esrange at 05:32 UT. The calibration of the rotational-Raman backscatter signal was done for measurements averaged between 04:23 and 05:53 UT. Figure 3c shows the deviation between the lidar profile and the radiosonde and the statistical temperature uncertainties of the lidar measurements. The calibration can only be performed when the radiosonde and the lidar measurements are close in space and time. In the case presented here the reference data for the calibration were taken below an altitude of 15 km. The horizontal distance of the radiosonde to the launch side at Esrange was 38.5 km at an altitude of 15 km. The derived temperature profile is in agreement with the ECMWF-reanalysis from 06:00 UT up to an altitude of 25 km (Fig. 3b). The statistical uncertainty of the derived temperature profile (grey area in Fig. 3b) is below 1 K up to an altitude of 15 km. Between 15 and 30 km the statistical uncertainties reaches values up to 2 K.

4 Application to PSC and cirrus measurements

Figure 4 shows that combining the findings of the measurements of the new rotational-Raman channels (black) with the integration technique (blue) allows for a retrieval of temperature profiles between 5 and 80 km. The temperature profile was measured between 13:39 UT on 14 January 2011 and 08:36 UT on 15 January 2011. Very good agreement is found in the overlap region of the two techniques between altitudes of 28 and 32 km. However, below 28 km the temperature profile derived by using the integration technique gives lower values (more than 5 K difference). The reason for this temperature difference is that the integration technique is only reliable within an aerosol-free atmosphere above 30 km. For comparison temperature profiles measured by a radiosonde launched at 13:30 UT the same day (red) and derived from ECMWF reanalysis (green) are shown in Fig. 4 as well. The temperature profiles obtained with lidar, radiosonde, and from the model output are in very good agreement. Temperature differences of 1 K and 2 K are found below and above the tropopause, respectively.

AMTD

5, 6455–6478, 2012

We will give two examples of how the new rotational-Raman channels improve the measurement capabilities of the Esrange lidar. The first is an application to PSC measurements while the second deals with the observation of a sub-visual cirrus cloud.

Figure 5a shows the development of a PSC observed between 19:48 and 01:23 UT on 6/7 February 2011 above Esrange. The PSC-types were routinely classified depending on their perpendicular and parallel backscatter ratios as described by Blum et al. (2005). According to this classification the observed PSC consisted of a layer with a mixture of solid and liquid STS particles between 19 and 22.5 km topped by a pure NAT layer between 22.5 and 23.5 km. Between 21:30 and 01:00 UT a mixed-phase layer that descended from 18.5 km down to 16 km was observed.

Further, Fig. 5b shows the lidar-derived temperature profile integrated over the entire measurement period together with formation and existing temperatures for the different types of PSCs. The temperature was calculated with the calibration constants derived from the measurements on 20 January 2011, discussed in Sect. 3. PSCs of type Ib (STS) form at temperatures below 193 K which were reached between 19 and 21.5 km. In contrast, PSCs of type Ia (NAT) and II (ice) are initiated at temperatures 3–4 K below the ice frost point. This threshold was not reached during the measurement period. However, the temperature was below the NAT existence temperature of 195 K between 17.5 and 24 km. The latter two facts suggest that the NAT layers observed in the classification presented in Fig. 5a were not formed over the measurement site.

A development of a cirrus cloud is shown as change in the particle depolarization signal over time in Fig. 6a. The cirrus cloud was observed between 9.5 and 10.2 km from 14:31 to 17:45 UTC on 25 January 2012. The corresponding profiles of the extinction coefficient, the lidar ratio, and temperature are shown in Fig. 6b–d, respectively. The extinction coefficient reached a value of 60 Mm^{-1} in the cirrus cloud. The corresponding lidar ratio of around 25 ± 3 sr is typical for sub-visual cirrus observations (Josset et al., 2012).

AMTD
5, 6455–6478, 2012

5 Conclusions and outlook

We have described the design of a pure rotational-Raman channel for atmospheric temperature and aerosol extinction measurements and its application to the Esrange lidar near Kiruna, Sweden. The new detection channel was optimized for temperature measurements between 180 and 200 K. This corresponds to the conditions in the lower Arctic stratosphere during winter. Using light reflected at the interference filter of the 532-nm elastic backscatter channel in combination with narrow-bandwidth interference filter in the rotational-Raman channels leads to a strong attenuation (more than 10 orders of magnitude) of the elastic backscatter signal and allows for the use of rotational-Raman lines close to the wavelength of the emitted laser light. This design minimizes the systematic error in the obtained temperature profile to less than 0.51 K. A reference profile from a radiosonde or meteorological reanalysis data are needed for an initial calibration of the lidar-derived temperature profile. No further calibration is necessary in case of a stable performance of the lidar system. By combining rotational-Raman measurements (5–35 km height) and the integration technique (30–80 km height), the Esrange lidar is now capable of measuring atmospheric temperature profiles from the lower troposphere to the mesosphere. The new capability of the instrument furthermore enables the study of temperature variations, aerosol extinction, lidar ratio, and small-scale structures in the upper troposphere/lower stratosphere region.

We have presented temperature profiles obtained with the new rotational-Raman channel during measurements on 20 January 2011 (no clouds, initial calibration) and 6 February 2011 (PSC, no further calibration). The temperature profiles generally show good agreement with both radiosonde and reanalysis output. We have presented temperature observations in a PSC in combination with its classification from polarization-sensitive elastic backscatter signals according to an established method. The temperature measurements support the classification of the different layers of the observed PSC. With the new detection system in place, a growing number of measurements, with combined PSC classification and temperature profiles within the PSC will now

AMTD
5, 6455–6478, 2012

be used to validate the current understanding of PSC formation and to improve common lidar-based PSC classification schemes. These studies will take advantage of the geographical location of Esrange where mountain wave activity in the lee of the Scandinavian mountain range gives rise to a wide range of PSC growth conditions. This is expected to lead to a better understanding of PSC formation, microphysics, and interactions.

Acknowledgements. We thank the MISU lidar team for operating the Esrange lidar and the Esrange personnel for their support during the measurement campaign. The rotational-Raman set up was financed by Esrange. The participation of M. Khaplanov was funded by SNSB. Further we thank U. Blum and K. H. Fricke for the fruitful discussions and ideas of how to improve the Esrange lidar system. We thank ECMWF for providing us with the model data used in this study.

References

Achtert, P., Khosrawi, F., Blum, U., and Fricke, K. H.: Investigation of polar stratospheric clouds in January 2008 by means of ground-based and spaceborne lidar measurements and microphysical box model simulations, J. Geophys. Res., 116, D07201, doi:10.1029/2010JD014803, 2011. 6459

Achtert, P., Karlsson Andersson, M., Khosrawi, F., and Gumbel, J.: On the linkage between tropospheric and Polar Stratospheric clouds in the Arctic as observed by space-borne lidar, Atmos. Chem. Phys., 12, 3791–3798, doi:10.5194/acp-12-3791-2012, 2012. 6458

Adhikari, L., Wang, Z., and Liu, D.: Microphysical properties of Antarctic polar stratospheric clouds and their dependence on tropospheric cloud systems, J. Geophys. Res., 115, D00H18, doi:10.1029/2009JD012125, 2010. 6458

Ansmann, A. and Müller, D.: Lidar and atmospheric aerosol particles, in: Lidar: Range-Resolved Optical Remote Sensing of the Atmosphere, edited by: Weitkamp, C., Springer, New York, 2005. 6462

Behrendt, A.: Temperature measurements with lidar, in: Lidar: Range-Resolved Optical Remote Sensing of the Atmosphere, edited by: Weitkamp, C., Springer, New York, 2005. 6457, 6461, 6463

Behrendt, A. and Reichardt, J.: Atmospheric temperature profiling in the presence of clouds with a pure rotational Raman lidar by use of an interference-filter-based polychromator, Appl. Optics, 39, 1372–1378, 2000.

Behrendt, A., Reichardt, J., Siebert, J., Fricke, K. H., and Weitkamp, C.: Tropospheric and stratospheric temperature measurements with lidar above Esrange in January and February 1999, Air Pollution Report 73, European Comission, 153–156, 1999. 6460

Behrendt, A., Nakamura, T., Onishi, M., Baumgart, R., and Tsuda, T.: Combined Raman lidar for the measurement of atmospheric temperature, water vapor, particle extinction coefficient, and particle backscatter coefficient, Appl. Optics, 41, 7657–7666, 2002. 6462

Blum, U. and Fricke, K. H.: The Bonn University lidar at the Esrange: technical description and capabilities for atmospheric research, Ann. Geophys., 23, 1645–1658, doi:10.5194/angeo-23-1645-2005, 2005. 6458, 6459, 6463

Blum, U., Fricke, K. H., Müller, K. P., Siebert, J., and Baumgarten, G.: Long-term lidar observations of polar stratospheric clouds at Esrange in Northern Sweden, Tellus B, 57, 412–422, 2005. 6457, 6465

Buchholtz, A.: Rayleigh-scattering calculations for the terrestrial atmosphere, Appl. Optics, 34, 2765–2773, 1995. 6462

Carslaw, K. S., Wirth, M., Tsias, A., Luo, B. P., Dörnbrack, A., Leutbecher, M., Volkert, H., Renger, W., Bacmeister, J. T., Reimers, E., and Peter, T. H.: Increased stratospheric ozone depletion due to mountain-induced atmospheric waves, Nature, 391, 675–678, 1998. 6457

Cooney, J.: Measurement of atmospheric temperature profiles by Raman backscatter, Appl. Meteorol., 11, 108–112, 1972. 6458

Dörnbrack, A., Leutbecher, M., Reichardt, J., Behrend, A., Müller, K. P., and Baumgarten G.: Relevance of mountain wave cooling for the formation of polar stratospheric clouds over Scandinavia: mesoscale dynamics and observations for January 1997, J. Geophys. Res., 106, 1569–1581, 2000. 6457

Faduilhe, D., Keckhut, P., Bencherif, H., Robert, L., and Baldy, S.: Stratospheric temperature monitoring using a vibrational Raman lidar, Part 1: Aerosols and ozone interferences, J. Environ. Monitor, 7, 357–364, doi:10.1039/B415299A, 2005. 6458

Gumbel, J.: Atmospheric science with sounding rockets – present status and future perspectives, in: Proc. 18th ESA Symposium on European Rocket and Balloon Programmes and Related Research, ESA SP-647, 47–54, 2007. 6459

AMTD

5, 6455–6478, 2012

Rotational-Raman channel of Esrange lidar

P. Achtert et al.

Title Page
Abstract | Introduction
Conclusions | References
Tables | Figures
◀◀ | ▶▶
◀ | ▶
Back | Close
Full Screen / Esc

Printer-friendly Version
Interactive Discussion

Hauchecorne, A., Chanin, M. L., Keckhut P., and Nedeljkovic, D.: LIDAR monitoring of the temperature in the middle and lower atmosphere, Appl. Phys. B, 55, 29–34, doi:10.1007/BF00348609, 1992. 6458

Höpfner, M., Blumenstock, T., Hase, F., Zimmermann, A., Flentje, H., and Fueglistaler, S.: Mountain polar stratospheric cloud measurements by ground based FTIR solar absorption spectroscopy, Geophys. Res. Lett., 28, 2189–2192, 2001. 6457

Josset, D., Pelon, J., Garnier, A., Hu, Y., Vaughan, M., Zhai, P.-W., Kuehn, R., and Lucker, P.: Cirrus optical depth and lidar ratio retrieval from combined CALIPSO–CloudSat observations using ocean surface echo, J. Geophys. Res., 117, D05207, doi:10.1029/2011JD016959, 2012. 6465

Juárez, M. D., Marcus, S., Dörnbrack, A., Schrøder, T. M., Kivi, R., Iijima, B. A., Hajj, G. A., and Mannucci, A. J.: Detection of temperatures conducive to Arctic polar stratospheric clouds using CHAMP and SAC-C radio occultation data, J. Geophys. Res., 114, D07112, doi:10.1029/2008JD011261, 2009. 6457

Keckhut, P., Chanin, M. L., and Hauchecorne, A.: Stratosphere temperature measurement using Raman lidar, Appl. Optics, 29, 5182–5186, doi:10.1364/AO.29.005182, 1990. 6458

Khosrawi, F., Urban, J., Pitts, M. C., Voelger, P., Achtert, P., Kaphlanov, M., Santee, M. L., Manney, G. L., Murtagh, D., and Fricke, K.-H.: Denitrification and polar stratospheric cloud formation during the Arctic winter 2009/2010, Atmos. Chem. Phys., 11, 8471–8487, doi:10.5194/acp-11-8471-2011, 2011. 6459

McCormick, M. P., Steele, H. M., Hamill, P., Chu, W. P., and Swissler, T. J.: Polar stratospheric cloud sightings by SAM II, Atmos. Sci., 39, 1387–1397. 1982. 6457

Nedeljkovic, D., Hauchecorne, A., and Chanin, M.-L.: Rotational Raman lidar to measure the atmospheric temperature from ground to 30 km, IEEE T. Geosci. Remote, 31, 90–101, 1993. 6460

Poole, L. R. and McCormick, M. P.: Airborne lidar observations of Arctic polar stratospheric clouds: indication of two distinct growth stages, Geophys. Res. Lett., 15, 21–23, doi:10.1029/GL015i001p00021, 1988. 6457

Radlach, M., Behrendt, A., and Wulfmeyer, V.: Scanning rotational Raman lidar at 355 nm for the measurement of tropospheric temperature fields, Atmos. Chem. Phys., 8, 159–169, doi:10.5194/acp-8-159-2008, 2008. 6460, 6461

AMTD
5, 6455–6478, 2012

Rotational-Raman channel of Esrange lidar

P. Achtert et al.

Wang, Z., Stephens, G., Deshler, T., Trepte, C., Parish, T., Vane, D., Winker, D., Liu, D., and Adhikari, L.: Association of Antarctic polar stratospheric cloud formation on tropospheric cloud systems, Geophys. Res. Lett., 35, L13806, doi:10.1029/2008GL034209, 2008. 6458

AMTD

5, 6455–6478, 2012

Rotational-Raman channel of Esrange lidar

P. Achtert et al.

Table 1. Emitter properties and characteristics such as central wavelength (CWL), full width at half maximum (FWHM) of the receiver branches.

emitter			
wavelength, nm		532	
polarization		linear	
beam diameter, mm		90	
beam divergence, µrad		50	
puls energy, mJ		350	
receiver			
channel, nm	532 ⊥	532 ‖	608
CWL, mm	532.13	532.13	608.36
FWHM, nm	0.12	0.13	3.00
altitude range, km	4–100	4–60	4–50

AMTD
5, 6455–6478, 2012

AMTD
5, 6455–6478, 2012

Table 2. Filter parameters (angle of incidence (AOI), central wavelength (CWL), full width at half maximum (FWHM)) used in the new rotational-Raman receiver branch. The values are taken from manufacturer's data sheet (Barr Associates, MA, USA).

	R-IF1	R-IF2
AOI, deg	4.5	1
CWL, nm	529.45	531.55
FWHM, nm	1.2	0.5
peak transmission, %	>80	>70
band blocking a 532 nm, orders of magnitude	>8	>8

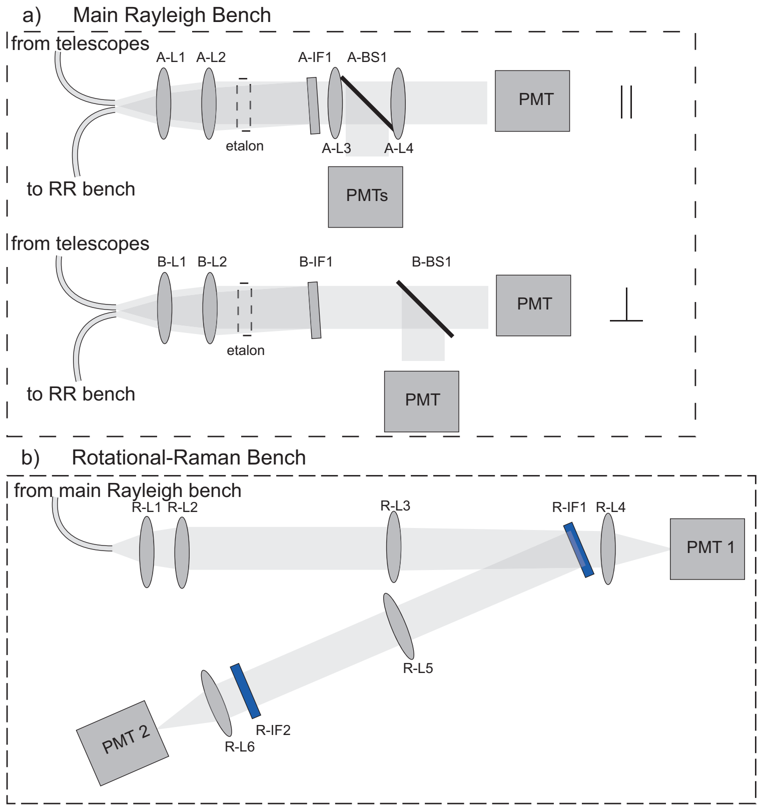

Fig. 1. Schematic setup of the pick-up and the rotational Raman (RR) bench. **(a)** The pick-up of the rotational-Raman signal in the main Rayleigh bench is based on the reflected light from the interference filters (A-IF1,B-IF1). This is shown for both parallel (**a**, upper schema) and perpendicular (**a**, lower schema) optical bench. **(b)** Setup of the rotational Raman bench. IF: interference filter (blue: rotational-Raman filter), L: lenses, BS: beam splitter. The parameter for the interference filters of the rotational-Raman channel are given in Table 2.

AMTD
5, 6455–6478, 2012

Rotational-Raman channel of Esrange lidar

P. Achtert et al.

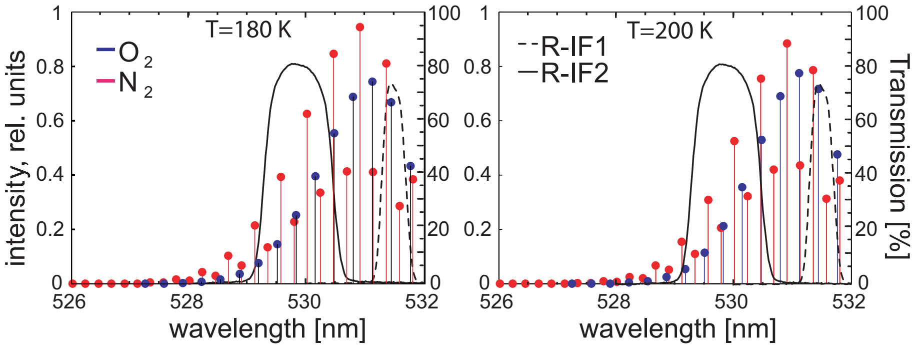

Fig. 2. The line-by-line pure rotational-Raman spectrum (only anti-Stokes) of O_2 (blue) and N_2 (red) calculated for $T = 180\,K$ (left) and $T = 200\,K$ (right) and the transmission curve of the two interference filters (R-IF1 with a central wavelength line (CWL) at 531.55 nm and R-IF2 with a CWL at 529.35 nm) produced by Barr Associates, Inc.

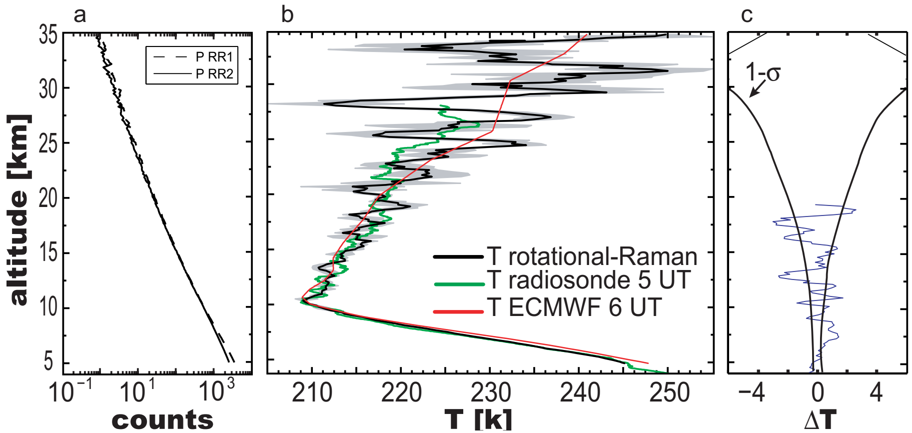

Fig. 3. Temperature measurements at Esrange between 03:17 and 07:58 UT on 20 January 2011. **(a)** Raw counts of the two rotational-Raman channels. **(b)** Atmospheric temperature profile calculated from the rotational-Raman signal (black, grey area shows the error) in comparison to the temperature profile from a radiosonde launched at 05:00 UT from Esrange (green) and the ECMWF-reanalysis temperature profile (red) from 06:00 UT. **(c)** Deviation between the lidar profile and the radiosonde (blue) as well as the statistical temperature uncertainties of the lidar measurements (black).

AMTD
5, 6455–6478, 2012

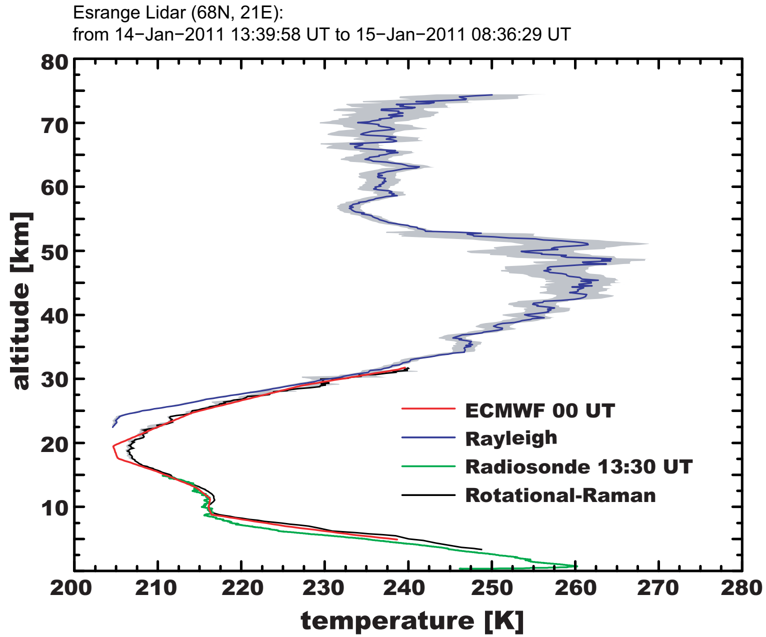

Fig. 4. Temperature profile between 5 and 75 km measured at Esrange between 13:39 UT on 14 January 2011 and 08:36 UT on 15 January 2011. Profile were obtained using the integration technique (blue) and the rotational-Raman technique (black). The grey shaded area shows the error range. For comparison the temperature profiles measured with radiosonde (green) and given by the ECMWF re-analysis (red) are shown as well.

AMTD
5, 6455–6478, 2012

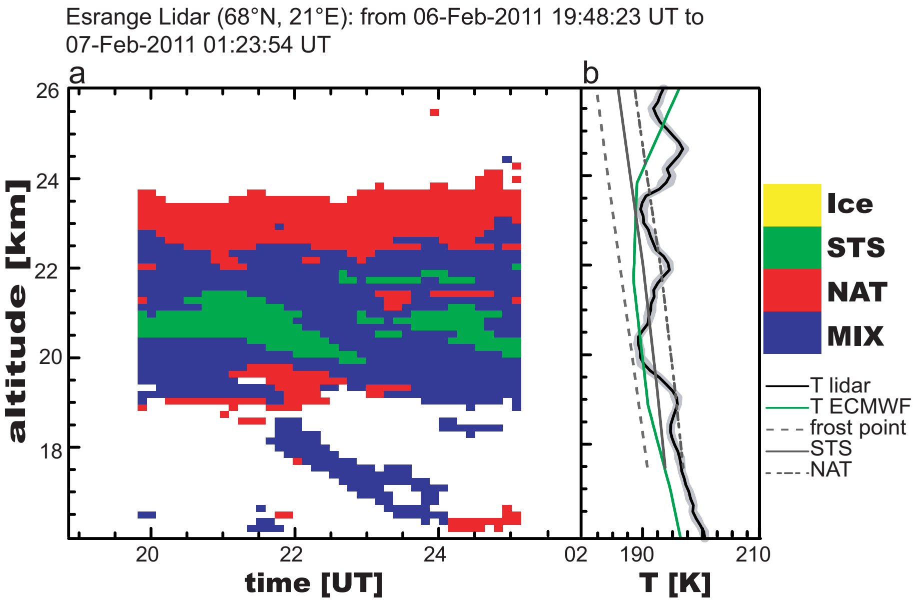

Fig. 5. **(a)** Development of a PSC above Esrange on 6 February 2011 between 19:48 and 01:23 UT. **(b)** Temperature profile (black) and the error in the temperature (grey area) derived over the entire measurement period in comparison to ECMWF from 00:00 UT on 7 February 2011. Grey lines indicate the formation and existing temperatures for PSC of type: ice (dashed), STS (solid), and NAT (intermittent).

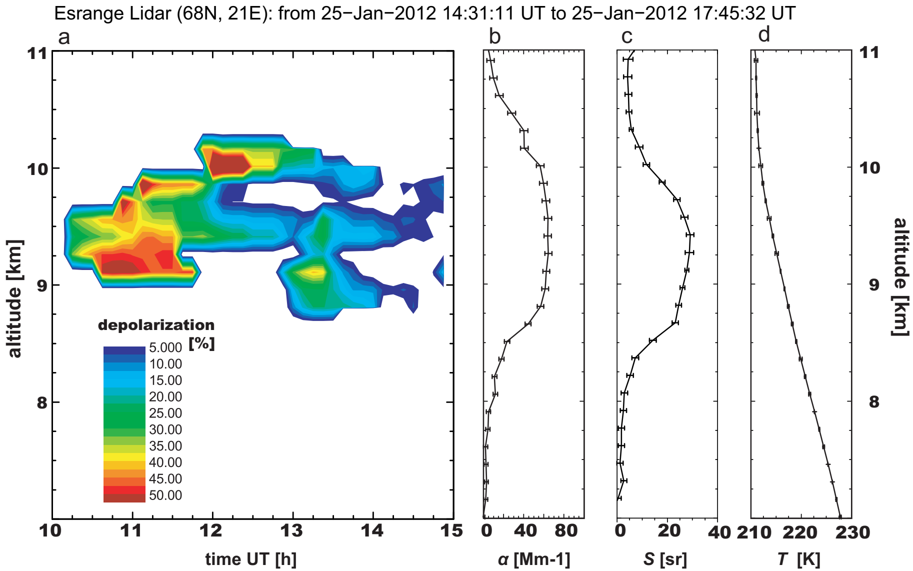

Fig. 6. (a) Development of a cirrus cloud above Esrange between 14:31 and 17:45 UT on 25 January 2012 in terms of the particle depolarization ratio and profiles of the extinction coefficient α **(b)**, the lidar ratio S **(c)**, and temperature T **(d)**.

AMTD
5, 6455–6478, 2012

Rotational-Raman channel of Esrange lidar

P. Achtert et al.